Available online at www.sciencedirect.com
ScienceDirect
Earth and Planetary Science Letters 261 (2007) 49–64
EPSL
www.elsevier.com/locate/epsl

Defining the source region of the Indian Ocean Tsunami from GPS, altimeters, tide gauges and tsunami models

Julie Pietrzak [a,*], Anne Socquet [b,1], David Ham [a,c], Wim Simons [d], Christophe Vigny [e], Robert Jan Labeur [a], Ernst Schrama [d], Guus Stelling [a], Deepak Vatvani [f]

[a] CiTG, Delft University of Technology, Stevinweg 1, 2628 CN Delft, The Netherlands
[b] EES Department, University of California Los Angeles (UCLA) 90095-1567 California, USA
[c] ESE Department, Imperial College London, SW7 2AZ, UK
[d] DEOS, Delft University of Technology, Kluyverweg 1, 2629 HS Delft, The Netherlands
[e] Laboratoire de Geologie, ENS/CNRS, 75231 Paris, France
[f] Delft Hydraulics, P.O. Box 177, 2600 MH, Delft, The Netherlands

Received 2 April 2007; received in revised form 4 June 2007; accepted 4 June 2007
Available online 12 June 2007
Editor: M.L. Delaney

Abstract

To understand the role of the co-seismic moment magnitude, M_w, 9.1–9.3 Sumatra–Andaman Earthquake rupture mechanism on the severity of the Indian Ocean Tsunami, we used permanent Global Positioning System (GPS) data and carried out an analysis of co-seismic displacement and tsunami models. Tsunami modelling, validated against independent Jason-1 altimetry data and tsunami arrival time data as determined from tide gauges, was used to analyse the results of five co-seismic slip inversions, using GPS, seismicity and/or uplift data. In this way we determined the most likely slip distribution characterized by slip maxima of ~20 m in the South and ~20 m in the North. We used both the distribution and temporal evolution of the co-seismic slip as derived from the GPS data. We show that the ~9 min propagation time of the rupture led to constructive interference of waves radiating first from the South and minutes later from the North, strengthening the tsunami in Southern India, Sri Lanka and Thailand. We conclude that the incorporation of permanent real-time GPS stations would represent a valuable component of future tsunami warning systems.

Keywords: GPS; Sumatra–Andaman Earthquake; Indian Ocean Tsunami

1. Introduction

The Great Sumatra–Andaman Earthquake had a co-seismic moment magnitude (M_w) of 9.1–9.3, (Ammon et al., 2005; Stein and Okal, 2005). It occurred offshore of Sumatra in the subduction zone near the triple plate junction between India, Australia and Sundaland. In the Indian Ocean, the diffuse plate boundary between India

* Corresponding author. Tel.: +31 15 278 1953; fax: +31 15 2784842.
E-mail addresses: j.d.pietrzak@tudelft.nl (J. Pietrzak), socquet@ipgp.jussieu.fr (A. Socquet), david.ham@imperial.ac.uk (D. Ham), w.j.f.simons@tudelft.nl (W. Simons), vigny@geologie.ens.fr (C. Vigny), r.j.labeur@tudelft.nl (R.J. Labeur), e.j.o.schrama@tudelft.nl (E. Schrama), g.s.stelling@tudelft.nl (G. Stelling), deepak.vatvani@wldelft.nl (D. Vatvani).
[1] Now at IPGP, Laboratoire de Tectonique et Mecanique de la Lithosphere, 4 place Jussieu, 75005 Paris, France.

0012-821X/$ - see front matter © 2007 Elsevier B.V. All rights reserved.
doi:10.1016/j.epsl.2007.06.002

and Australia is a wide region, affected by NW–SE compressive deformation of the oceanic lithosphere (Chamot-Rooke et al., 1993), and by active left-lateral strike slip along north-trending paleo transform faults (Deplus et al., 1998; Deplus, 2001; Abercrombie et al., 2003). In the long term, the oblique convergence between the Indian Ocean and the Sundaland Block (Simons et al., in press) is accommodated by slip partitioning between two parallel, interseismically locked tectonic entities: the Sumatra–Andaman–Arakan subduction in the forearc and the Sumatra–Sagaing strike slip fault system in the back arc, (Fitch, 1972; Curray, 1989; McCaffrey, 1991; Prawirodirdjo et al., 1997; Genrich et al., 2000; McCaffrey et al., 2000; Nielsen et al., 2004; Socquet et al., 2006). The earthquake ruptured an 1100–1300 km long section of the subduction interface, starting from the northern edge of Sumatra and ending offshore from the Andaman Islands, (Banerjee et al., 2005; Bilham, 2005; Ishii et al., 2005; Krüger and Ohrnberger, 2005; Lay et al., 2005; Ni et al., 2005; Park et al., 2005; Subarya et al., 2005; Vigny et al., 2005; Briggs et al., 2006). It lasted for approximately 8–10 min (Ishii et al., 2005; Vigny et al., 2005), and generated one of the largest tsunamis of recent times (Lay et al., 2005; Titov et al., 2005a) causing colossal devastation and loss of life as it propagated into coastal regions without any tsunami warning being issued.

This earthquake is thought to have increased the stress and raised the seismic hazard on the adjacent segments of the subduction zone. The March 2005 M_w=8.7 Nias earthquake, Briggs et al. (2006) which occurred just south of the 2004 event, is an example of the triggered seismicity, there is now concern for at both ends of the rupture. To the north for example, offshore of the Myanmar coast, the Arakan Trench elastically accumulates a significant part of the relative motion between the Indian and Sundaland plates and is likely to produce a M_w=8.5 earthquake every century or a M_w=9 every 500 yr (Socquet et al., 2006). However, the risk of another devastating tsunami is not restricted to the Indian Ocean (Nedimovic et al., 2003; Titov et al., 2005b). The population explosion in coastal regions means that, more so than at any other time in our history, we are at risk from tsunami's resulting from submarine earthquakes.

An outstanding issue is the rapid and accurate determination of the spatial distribution of slip and its temporal evolution. This has direct implications for tsunami warning and will ultimately lead to a better understanding of earthquake rupture mechanisms and associated seismic hazards. The first estimates of the earthquake magnitude calculated from seismic data underestimated the magnitude of the earthquake, the length of rupture and hence the size of the tsunami. It took nine hours for seismologists to issue a M_w=9 estimate and ~450 km rupture length, but it took days to get a more accurate estimate of the magnitude and real rupture length. To address this issue, we present the first Indian Ocean Tsunami modelling results to use co-seismic uplift fields together with estimates, every 30 s, of the position of the rupture as derived from the kinematic analysis of permanent far field Global Positioning System (GPS) stations (Vigny et al., 2005). This analysis established that the rupture first propagated toward the north–north-west at a speed of ~3.5 kms^{-1} until 7–8° N, continuing farther north more slowly at ~2 kms^{-1} and that all co-seismic motion ceased within 10 min.

We demonstrate how tsunami model results, validated against the independent Jason-1 altimetry data and tide gauge arrival time data, can be used to select between the results of five co-seismic slip inversions. To our knowledge this is the first time GPS data have been used together with tsunami models to improve our estimates of the slip along a thrust-fault earthquake. Here, we use permanent GPS data to gain new insights into the earthquake rupture mechanism; in so doing we demonstrate that the SE Asia GPS network in place at the time of the 2004 Sumatra–Andaman Earthquake could have been used to issue a tsunami warning and that GPS should be part of future warning systems.

2. Methods

We run co-seismic displacement models and then use the results of tsunami models, validated against independent Jason-1 satellite altimeter data and tide gauge data, to assess the quality of the inversions. In the first step the GPS and uplift data, described in Vigny et al. (2005), Subarya et al. (2005), Gahalaut et al. (2006), and Bilham et al. (2005) are inverted to obtain the co-seismic slip distribution. In the second step uplift and subsidence fields are generated by a forward elastic model using the previously calculated slip on the fault. The uplift and subsidence fields are then used to generate the initial fields for tsunami simulations, using two unstructured mesh finite volume and finite element numerical models, Delfin and Finlab, described in Ham et al. (2005) and Labeur and Pietrzak (2005) respectively. The quality of the inversions is assessed by a comparison of the simulated sea surface displacements against those measured by Jason-1. In addition, a comparison is made between the simulated and recorded tsunami arrival times around the Bay of Bengal.

2.1. Co-seismic modelling from GPS data and uplift data

The estimation of the surface deformation due to slip on the fault was carried out with the Okada (1985, 1992) half-space dislocation algorithm. This is implemented in the inversion program DEFNODE (McCaffrey, 1995, 2002, 2005) which applies simulated annealing to downhill simplex minimization (Press et al., 1989) to solve for the model parameters. We minimize data misfit (between modelled and observed co-seismic displacements), defined by the reduced chi-squared statistic: $\chi^2_n = \frac{\sum(r^2/s^2)}{\mathrm{dof}}$ where r is the residual between model and observations, s is the standard deviation and dof is the degrees of freedom. The uplift field is generated by calculating every 0.2° of latitude, the surface deformation due to the slip on the fault, determined by the previous inversions. It should be noted that the inversions are static; we did not account for the timing of the rupture in the inversions, although this is possible in principle, see for example Bürgmann et al. (2002).

In the first model, published in Vigny et al. (2005) hereafter referred to as Model 1, the surface fault geometry follows the map published by Pubellier et al. (2003), the dip angle is fixed at 13° consistent with the USGS focal mechanism and a maximum depth of 50 km is assumed. The amount of slip on the fault is inverted at each node with the assumption of a uniform direction. With a normalised χ^2 of 2.2 and a weighted Root Mean Square (RMS) of 4 mm, this model was found to give the best agreement between modelled and observed deformation in an extensive analysis of the GPS data. This model leads to a seismic moment (Mo)=4.10^{22} N m, corresponding to a $M_w \sim 9.06$; if the rigidity values at depth are those defined in the Preliminary Reference Earth Model, (Dziewonski and Anderson, 1981). However, the location at the bottom edge of the fault of some patches of important slip does not seem realistic. The low moment magnitude is probably due to the fact that the fault interface is artificially stopped at 50 km depth. We will show here that substantial differences between modelled and observed tsunami arrival times led us to further investigate the slip distribution.

In all subsequent inversions (Models 2–5), we therefore use a refined geometry of the fault, for details see Fig. S1, Supplementary Material. The co-seismic slip direction on the fault is estimated by solving for the normalized angular velocities of two fore arc segments relative to Sunda. The angular velocities were constrained by GPS vectors and 314 slip vectors derived from aftershock seismicity (CMT focal mechanisms). Both normalized rotation axes comprise 4 free parameters. The amplitude of the co-seismic slip on the fault plane was fit as a Gaussian function of depth along 15 independent profiles across the margin (3 free parameters for each independent profile), following the method used by Subarya et al. (2005).

In Model 2 the same set of co-seismic, continuous GPS data as in Model 1, are inverted in order to test the effect of the fault geometry derived from seismicity and slip direction. We obtain a reduced chi-squared statistic of $\chi^2 = 2.8$ and a weighted RMS of 4 mm with respect to the GPS data. The slightly decreasing fit to the GPS data in this model with respect to Model 1 can be explained by the introduction of slip vector data that constrain the direction of the co-seismic slip that differs from the one inferred by GPS data only. This model leads to a Mo=$3.6\ 10^{22}$ N m, corresponding to a $M_w \sim 9.04$.

The moment magnitudes of Models 1 and 2 are too low when compared to those deduced from other independent geodetic models (Gahalaut et al., 2006; Chlieh et al., 2007). It is also smaller than that obtained by the latter authors if they invert the same set of data. This is because they minimize a cost function in their inversion, which includes a term of misfit to the supposed magnitude of 9.1. They also introduce a smoothing term which extends the surface of patches with significant slip and increases the magnitude. We didn't follow this approach.

In the third model presented here, Model 3, additional near field geodetic data are used in the inversion. In the south, GPS and uplift data at the latitude of northern Sumatra are used, Subarya et al. (2005). In the north, in the region of the Nicobar and Andaman Islands, campaign GPS published in Gahalaut et al. (2006) and uplift data published in Bilham et al. (2005) are used. Being located close to the fault zone, these data can help constrain the zones where slip actually occurred. However, unlike the continuous GPS data (Vigny et al., 2005) that are purely co-seismic, these near field data contain up to 2 months of post-seismic deformation. Consequently, these data should be carefully used and interpreted. In particular, campaign GPS data published in Gahalaut et al. (2006) claim a very small uncertainty, which has been increased by a factor 10 for the inversion. Whereas the uncertainties published in Subarya et al. (2005) were retained for the southern near field data. It should be noted that Banerjee et al. (2007) recently corrected the Gahalaut et al. (2006) data for the post-seismic contribution using an afterslip model. However, since the afterslip contribution may be extremely variable along the fault zone, here we use the original measurements and increase the error bar.

The co-seismic slip obtained for Model 3 corresponds to a $M_w \sim 9.13$ (Mo = 5 10^{22} N m), which is close to the magnitude given by seismic models (Ammon et al., 2005) and by some recent geodetic models (Gahalaut et al., 2006; Chlieh et al., 2007). However, the chi-squared statistic $\chi^2 = 15.1$ is worse, as is the weighted RMS of 37 cm with respect to the uplift data and 17 mm with respect to the GPS data. The fit of 9 mm to the far field purely co-seismic data is much better than the fit to the near field data (~27 cm to the data of Subarya et al. (2005) and ~1 m to the data of Gahalaut et al. (2006)). The difference of fit between the near field and the far field data has been obtained on purpose. Indeed, this model has been driven to fit in priority far field data to reflect the purely co-seismic motion.

In order to assess the influence of post-seismic deformation, Model 4 was run. This model only uses the near field data sets and seismicity as described above. The chi-squared statistic $\chi^2 = 4.1$ is better than in the previous model. This is due to a better fit to the near field data. The weighted RMS is 22 cm with respect to the uplift data and 8.5 cm with respect to the GPS data. The fit of 59 mm to the far field data, is substantially degraded with respect to the previous model. Whereas the fit to the near field data (~11 cm to the data of Subarya et al., 2005 and 0.6 m to the data of Gahalaut et al., 2006) is improved, by almost a factor 2, with respect to Model 3. This model leads to a Mo = 9.87 10^{22} N m and $M_w \sim 9.33$. This magnitude corresponds to almost twice the energy released according to Model 3 and is higher than any geodetic or seismologic model published (eg. Chlieh et al., 2007; Banerjee et al., 2007; Rhie et al., 2007). This is confirmed by the amplitude of the vectors predicted by the model, which is twice the one measured by the continuous GPS in Thailand and Malaysia.

As we will show, Model 3 produced a substantial improvement to the slip distribution in the south, but not in the north. Consequently we carried out Model 5. This model is identical to Model 2, except that it only uses the southern near field data, Subarya et al. (2005). The chi-squared statistic $\chi^2 = 8.2$ is improved, though it is not directly comparable to the χ^2 of other models. The weighted RMS is improved with respect to Model 3, both with respect to the uplift data (22 cm) and with respect to the GPS data (11 mm; being distributed between 9 mm to the far field purely co-seismic data and 23 cm to the near field data of Subarya et al. (2005)). This model gives a Mo = 4.1 10^{22} N m ($M_w \sim 9.08$), which is in agreement with, though slightly higher than, the one obtained for Models 1 and 2, purely co-seismic. The misfit to the near field data represents the post-seismic part of the measured vectors.

2.2. Numerical modelling

We used two unstructured mesh finite volume and finite element models, Delfin and Finlab, which here employ triangular elements. The unstructured mesh approach, has only recently been adopted for tsunami studies; although it is increasingly used in other modelling studies of the oceans and coastal zone, see Pietrzak et al. (2004, 2005) and references therein. It is also used in the German–Indonesian Tsunami Warning System, GITEWS (Schroeter et al., 2006) and in recent New Zealand tsunami studies (Walters, 2006). It offers the advantage of grid flexibility and the ability to better resolve coastlines and islands. Consequently we used high resolution (500 m) around the Andaman and Nicobar Islands, 1 km resolution on the Sumatra coast and parts of Thailand, through 10 km around Sri Lanka, to 20 km on northern parts of the Indian coast. The seaward most boundary of the domain to the south and west were sampled at 40 km resolution. The bathymetry comes from the General Bathymetric Chart of the Oceans (GEBCO) with a resolution of 1° latitude. Both Delfin and Finlab used the same mesh. Delfin is a hydrostatic model, whereas Finlab is a fully non-hydrostatic model. Finlab has the option to be run in a hydrostatic mode.

The temporal forcing of the seismically induced sea surface displacement was incorporated into the numerical tsunami simulations every 30 s. It was based upon the temporal evolution of the fault rupture as determined from the kinematic analysis (Vigny et al., 2005). The kinematic GPS analysis lists a set of points giving the position of the rupture every 30 s. We assumed a one to one correlation between the uplift and subsidence fields, and the sea surface perturbation. Based on these data sets we progressively perturbed the surface elevation at each time step in the first 9 min of the simulations with Delfin, as described in Ham (2006). In contrast, in the non-hydrostatic version of Finlab, the sea floor itself was ruptured, again according to this timing, and the model then calculates the evolution of the sea surface. A 30 s time step was used, in order to resolve the temporal evolution of the rupture.

In order to be sure the method of perturbing the sea surface did not influence the results we carried out a detailed comparison of the two codes, Delfin and Finlab using the uplift fields described in Ham (2006) (not presented here). The results from the two codes gave nearly identical results; both when we compared hydrostatic simulations from the two codes, as well as when we compared a hydrostatic and non-hydrostatic simulation. This gives us confidence that the method employed to

perturb the sea surface in Delfin, was as accurate as rupturing the sea floor itself (as simulated in Finlab). In addition, the influence of non-hydrostatic effects was found to be negligible for the large scale bed displacements studied here. Therefore only the results from the Delfin software are presented in the following.

2.3. Satellite altimeters and tide gauge data

Delft University of Technology and the National Oceanographic and Atmospheric Administration maintain a common Radar Altimeter Database system from which the Jason-1 altimeter data were extracted. Fig. 1 shows the bathymetry of the Indian Ocean, the location of the tide gauges and the track taken by the Jason-1 altimeter as it passed from south to north across the Indian Ocean. From this track we produced relative sea level data by taking differences between track 129 within cycle 109 that traversed the region on December 26th 2004 and a similar track observed 10 days earlier in cycle 108 on December 16th 2004. Furthermore we compared the results of taking differences between cycle 109 and 108, 109 and 107 and 109 and 106. We found negligible differences in the results, supporting our confidence in the Jason-1 data. We also discuss the TOPEX/Poseidon (T/P) satellite altimeter data. However, due to acquisition problems it has extensive gaps, which are described in Gower (2007). The better data coverage of Jason-1 provides estimates of the incident tsunami wave amplitudes and arrival times in deep water, as well as information on reflected waves. It took over 9 min for the Jason-1 altimeter to traverse the Indian Ocean. Consequently the transit time of the altimeter has to be taken into account in order to avoid potential timing errors. It is necessary to extract the discrete tsunami model data at the same position and time as that at which the altimeter data were recorded. Therefore, the surface elevation data calculated by the tsunami model were interpolated in time and space to correspond to the instantaneous measurements in the satellite track.

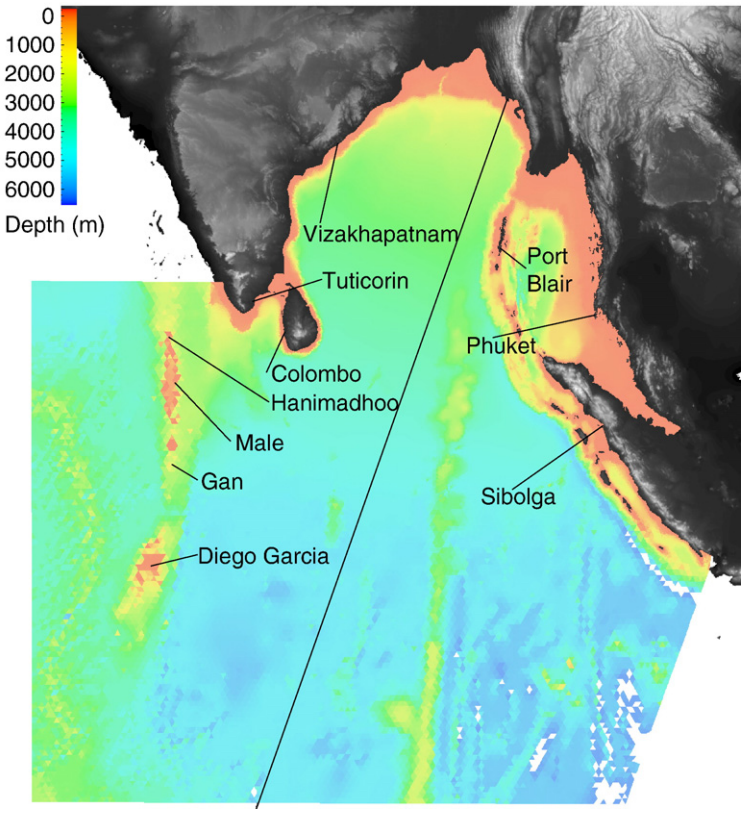

Fig. 1. The bathymetry of the Indian Ocean based on the GEBCO data set. The track taken by the Jason-1 satellite is shown, as are the locations of the tide gauges. Modelled arrival times are sensitive to the accuracy with which the bathymetry is known. Tsunami waves, travel with a phase speed given by $c = \sqrt{gH}$, where g is gravitational acceleration and H is the local water depth. In a depth of 4000 m, it takes 2 h to travel 1440 km. For much of the Jason-1 track we expect fairly good agreement between modelled and observed arrival times. However, the phase errors will increase in areas with substantial shallow regions, for example, the waves slow dramatically due to the topography in the Andaman Sea.

In the following, we carry out a detailed comparison of the numerical model results against the amplitude and phase of the incident tsunami waves recorded by the Jason-1 altimeter. We do not use an RMS error measure because it penalises phase errors, which as we will show provide valuable information about the slip distribution. We use T/P data, where available, to further support our findings. Finally we compare the model results with arrival times as recorded at the coast. The tide gauge data are now known to a fairly high level of accuracy, see for example, Merrifield et al. (2005), Rabinovich and Thomson (2007), Wijeratne and Pattiarachi (2005), Pattiarachi (2005), and are summarised in Table 1. However, we do not use waveforms as employed in Fujii and Satake (2007), since our resolution of bathymetry near the coasts is too coarse. Here we use information about the incident waves, as revealed by altimeter data and tide gauge arrival time data, to help identify the source region of the Indian Ocean Tsunami.

3. Results

3.1. Slip distribution from GPS data

A pronounced dual source region dominates the slip distribution of Models 1, 2 and 5 (Figs. 2 and S2 Supplementary Material). The two distinct patches of large slip, one in the south and one in the north, are separated by a zone with little or no slip at 7–8° N in Models 1 and 2, and at 5.5–7° N in Model 5. In contrast the slip distributions of Models 3 and 4 are quite different. They correspond to the longest ruptures produced by the inversions, over 1500 km long; populated by five to six patches of high slip distributed along the length of the rupture. Compared with Model 2, both rupture zones extend 1° farther south and 4° farther north, in agreement with the area affected by aftershock seismicity. Model 3 also consists of a southern and northern region of slip, but with a minimum at ~5–6° N.

The influence of the geometry, of the fault interface, is to emphasise the dual nature of the source region in Model 2 (Fig. 2) compared with Model 1 (Fig. S2). Furthermore, the southern patch of slip extends farther south-westwards in Model 2; note the extensive patch of ~20 m slip from 3–5° N, with a weaker patch of ~5 m slip extending northwards to 7° N. In the north, a significant patch of slip extends from 8–10° N, with slip of ~25 m centred at 9° N. The effect of including the near field data in Model 3 is substantial, Fig. 2. The dual source is now far less pronounced and the slip minimum is located 1° farther south. In terms of the distribution of the co-seismic slip along strike, the current

Table 1
Observed and modelled tsunami arrival times

Site	Co-ordinates	Sampling interval of tide gauge (min)	Arrival times of the leading incident tsunami waves (in minutes since the earthquake started)									
			Tide gauge	Model 1	Model 2	Model 2 South	Model 2 North	Model 3	Model 3 South	Model 3 North	Model4	Model5
Sibolga Indonesia	01.75° N; 98.75° E	3	107	82	97	97	162	86	86	144	80	81
Tuticorin India	08.75° N; 78.20° E	6	205	207	208	209	208	204	206	204	194	206
Vizakhap-atnam India	17.65° N; 83.28° E	5	156	136	150	168	150	132	185	132	130	152
Colombo Sri Lanka	06.93° N; 79.83° E	2	170	165	162	162	163	157	165	157	153	162
Male Maldives	04.18° N; 73.52° E	4	195	191	192	192	195	190	194	190	183	193
Diego Garcia UK	07.30° S; 72.38° E	6	226	217	207	207	225	208	208	216	203	207
Hanimad-hoo Maldives	06.77° N; 73.18° E	2	211	212	212	212	212	205	217	205	201	212
Gan Maldives	00.68° S; 73.17° E	4	197	195	192	192	197	194	194	194	184	194
Port Blair India	11.68° N; 92.77° E	2	15	18	16	66	16	12	83	12	15	17

Tsunami arrival times in minutes after the start of the earthquake, recorded at each of the tide gauges listed, and as modelled for Models 1–5 and Models 2 and 3 Southern and Northern ruptures. The name and co-ordinates of each tide gauge used, as well as the sampling interval are given in the table. The tide gauge data are based on the extensive analysis conducted by Rabinovich and Thomson (2007). If there was a significant increase or decrease in water level between two observation points, they assumed that the actual arrival time was midway between the adjacent points at which the change occurred. Note the time of arrival of the first wave at Mutwal fishery harbour Colombo is given above. See also Pattiarachi (2005) for a detailed discussion of the Columbo tide gauge. While the tide gauge data are now known to within 3–6 min it should be noted that the modelled arrival times at the coast are only accurate to within about 5–10 min; due to grid resolution and or unknown bathymetry in the coastal zone. First estimates of the Sibolga data (Merrifield et al., 2005; Vatvani et al., 2005) were based on analog records digitised for the tsunami event, with sampling intervals of 10 min. More recently the records were re-digitised and made available to Rabinovich and Thomson (2007). However, the modelled arrival times at Sibolga are less conclusive; all arriving too early. This likely reflects poorly resolved bathymetry and or physics in this area.

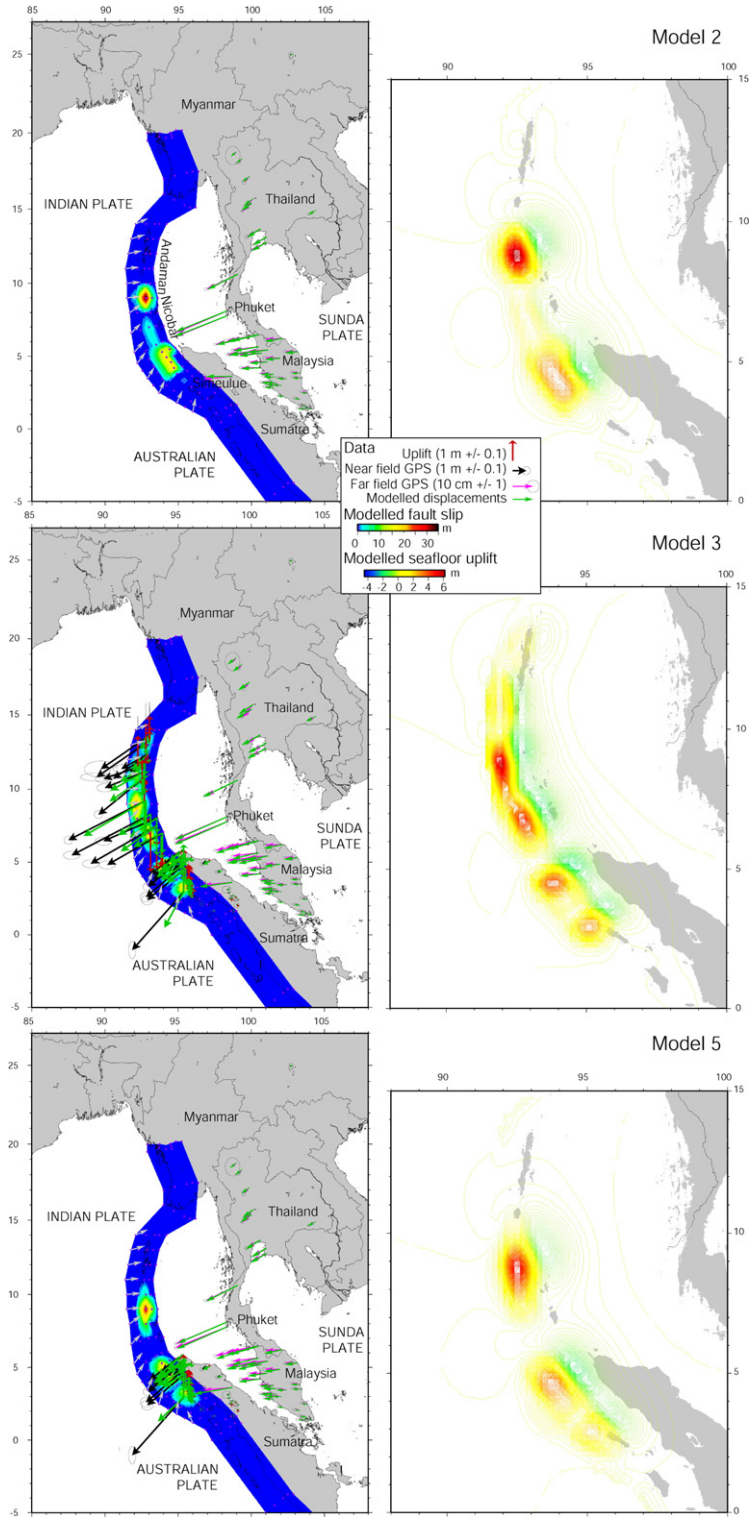

Fig. 2. Co-seismic slip distribution (left) and uplift and subsidence fields (right) for Models 2, 3 and 5. Comparison of measured (purple vectors) co-seismic horizontal displacements from the far field GPS data with the modelled deformations (green vectors) are also shown. Models 2 and 5 invert two large patches of slip in the south and north, located at ~3–5° N and 8–10° N (Model 2) and at ~2–5° N and 7–11° N (Model 5), separated by a zone with no or minimum slip at 7–8° N and 5.5–7° N, respectively. Note the more southern extension of the uplift and subsidence in Model 5. Model 3 inverts a much longer rupture with slip from 2.5° N to 13°N, and a minimum located at ~5–6° N. The amount of slip decreases from 10 m at 10° N to a few meters at ~14° N.

model is however in agreement with published models (Gahalaut et al., 2006; Chlieh et al., 2007; Banerjee et al., 2007; Rhie et al., 2007); with a patch of important slip between 3–5° N and another one, with smaller slip, between 6–10° N. The amount of slip decreases to a few meters at ~14° N. The near field data both increase the length of the rupture by over 500 km and the energy released by of the earthquake. However, it decreases the fit to the co-seismic far field data, (Fig. 2 and Section 2.1).

Model 4 displays a fairly continuous rupture with six distinct patches of slip, at the locations where there are data to infer it. The largest difference between the modelled and observed co-seismic vectors is found for this inversion, Fig. S2. However, the influence of the near field data can be observed; it forces the patch of slip in the far south at 2° N, as well as the patch of slip in the far north at 14° N. Neither source is reproduced by the far field co-seismic data alone. Notably the near field data also force slip at 5–6° N, where we otherwise find a minimum in Model 3. Furthermore, Model 3 is the only model to invert a slip maximum from 6–8° N. The slip distribution of Model 5 is similar to Model 2. However, the influence of the southern near field data is to extend the southern and northern patches of slip 1° farther south and 1° farther north. The obtained uplift and subsidence fields used for the tsunami modelling show a bipolar geometry (subsidence to the east and uplift to the west) in Fig. 2 and S2. The regions of largest uplift and subsidence occur where there is maximum slip on the fault interface.

3.2. Tsunami modelling

The best overall visual agreement, between the modelled sea surface displacements and the Jason-1 satellite altimetry data, in both the south-west (1700–2400 km) as well as the north-east of the track (3900–4800 km), is found for Models 2 and 5, Fig. 3A. Model 3 has the best visual agreement with the leading tsunami waves in the south-west of the domain. Conversely, Model 4 has the worst overall agreement; yet notably it is the only model to reproduce the peak at ~1900 km. Model 1 has the worst visual agreement with the incident waves in the south-west of the domain. However, the agreement in the north-east is as good as Models 2 and 5. It should be noted that Models 1 to 5 correspond to their respective slip inversions which have the same names, Models 1 to 5, respectively.

Models 2 and 5 underestimate the amplitude of the leading tsunami waves (at ~1900, 2000 and 2050 km) by over 50%, and instead of two peaks there is only one centred at the location of the trough at ~2000 km. In contrast the trough at ~2250 km is well represented, as is the peak at ~2400 km, with amplitude and phase errors of about 10%. In the north, the peak at 4700 km, the trough at 4400 km and the peak at 4200 km are reproduced with phase and amplitude errors of only 5–10%. Moreover the broad trough from ~2900–3900 km in the Bay of Bengal is reproduced, with amplitude and phase errors of ~10% from ~3300 km to ~3800 km. While the addition of the southern near field data in Model 5, did extend the location of the rupture farther to the south, the results are similar to Model 2. This is further supported by a comparison with the leading peak in the T/P data, Fig. S3, Supplementary Material.

In contrast, Model 3 is the only model to reproduce the double peak feature (at ~1900, 2000 and 2050 km), although its amplitude is ~50% of that observed and there are phase errors, with the simulated peak, trough, peak sequence located at ~2000, 2050 and 2100 km. The trough (~2250 km) is well reproduced in both amplitude and phase (within 10%). While the peak (~2400 km) and trough (~2450 km) are not reproduced, the broad peak from ~2600–2900 km is captured. In marked contrast the visual agreement with the recorded waves in the north, is the worst of all the simulations except for Model 4. Note T/P records the leading wave in the south-west as one broad peak, instead of the double peak recorded by Jason-1, as does Model 3; and Model 3 exhibits the same phase lag.

In either Model 3 or 4 there is no obvious peak, trough, peak sequence at ~4700, 4400 and 4200 km. In addition the broad trough from 2900–3900 km is replaced by a series of peaks. The patch of slip (~10 m) in the Andaman Islands in Models 3 and 4, corresponding to offshore uplift (~3 m), degrades the agreement with the northern incident waves. The poor visual agreement in Model 4 likely highlights the contamination of these data by post-seismic movements. Note however, that the peak at ~1900 km is only ~20% broader than the Jason-1 signal and the amplitude agrees within a few percent. When compared with T/P the results are consistent; a similar leading phase error although the amplitude is now somewhat over estimated. However, it appears the broad peak recorded by T/P is made up of the two leading waves recorded by Jason-1; with Model 4 capturing the first peak in Jason and the first half of the broad wave in T/P. Finally it is worth commenting that while the leading wave of Model 1 has a significant phase error, corresponding to an arrival time delay of ~6 min, the results from Model 1 could have been used to issue a reliable tsunami warning, Movie 1 Supplementary Material.

An analysis of the animations of Model 2 (Movies 2–4, Supplementary Material) indicates, that the peak at ~1900 km, trough at ~2000 km, the peak at ~2050 km

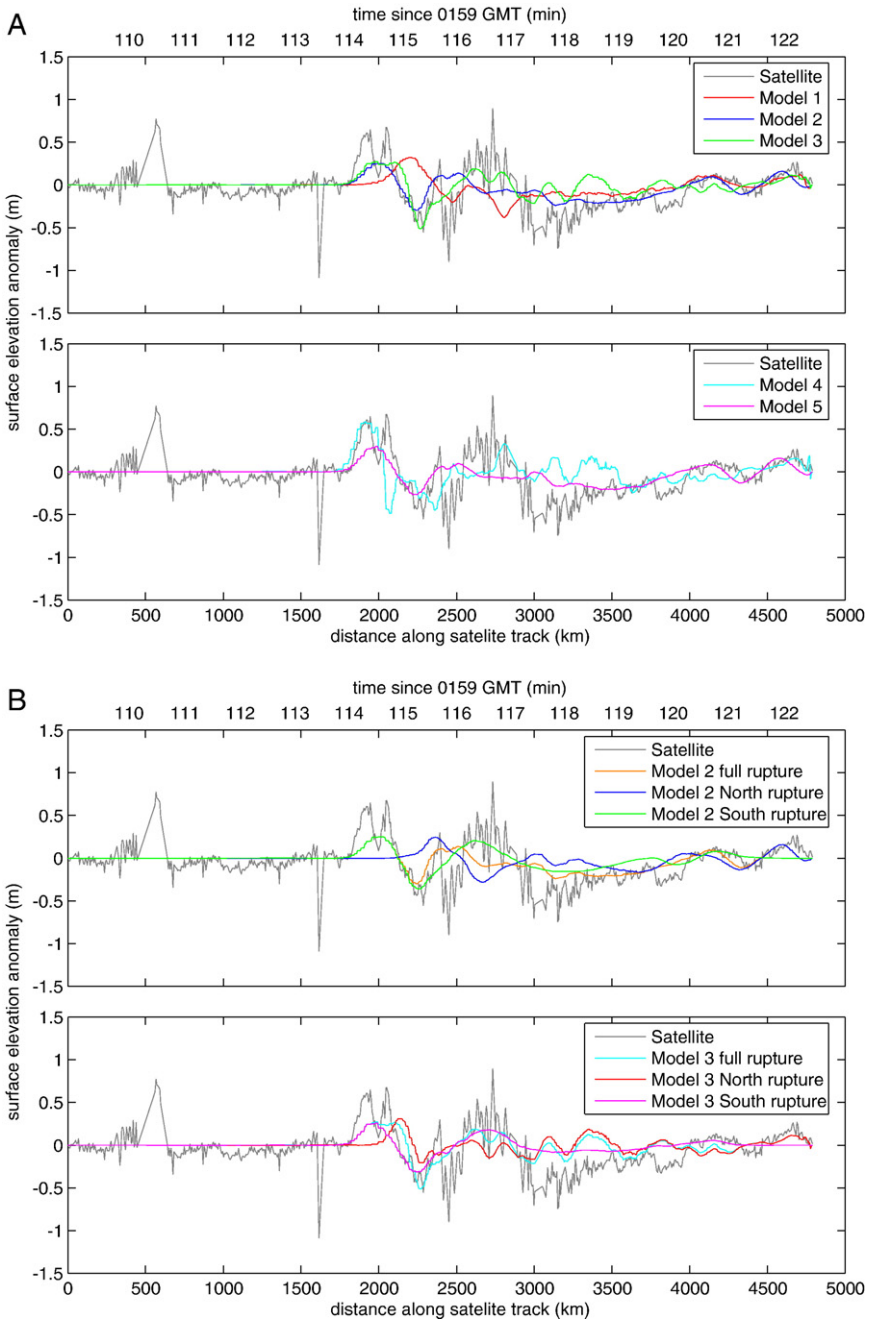

Fig. 3. Comparison of modelled against observed sea surface elevation anomaly. (A) For Models 1 to 5 and (B) for Models 2 and 3 northern and southern ruptures only. The Jason-1 altimeter data are shown in black. The start time of the south-western most part of the track was 1:53:48 (0 km) and the end time of the north-eastern most part of the track was 2:03:18 (~4800 km). The track intersects the leading waves of the tsunami in the south at 1:55 (~1900 km) whereas the leading wave in the north intersected the track at ~2:03 (~4700 km). Note the data spikes at ~550 km and ~1600 km. Time in minutes since the earthquake initiated is also shown. The RMS error of the altimeter data is about 0.02–0.03 m, while the timing is accurate to a thousandth of a second. Model 1 exhibits a substantial phase delay in the arrival of the leading wave in the south-west. Models 2 and 5 generate one peak instead of the double peak, whereas Model 3 reproduces the double peak but with a phase lag. Models 1, 2 and 5 reproduce the northernmost incident peak and trough, at ~4700 and 4400 km, which are only captured if the northern rupture data are included in Model 2. Models 3 and 4 do not reproduce the northern peak, trough, peak sequence. Model 2 indicates that the southernmost patch of slip is responsible for the simulated peak at ~2000 km, as well as reproducing the reflected peak from ~2600–2900 km. Notably the interference, of the waves from the south and north, degrades the solution between 2600–2900 km. The peak at ~4200 km appears to be due to the superposition of an incident wave from the southern patch of slip, interacting with a wave from the northern patch of slip.

and the trough at ~2250 km in the south-west, as well as the peak at ~4700 km, trough at ~4400, and the peak at ~4200 km in the north-east of the Jason-1 track, are incident waves. Whereas the third peak at ~2400 km, the broad peak from ~2600–2900 km and the broad trough from ~2900–3900 km in the Bay of Bengal are due to reflection and diffraction from Sumatra and the Nicobar and Andaman Islands. Any incident waves originating from sources near the Andaman and Nicobar Islands would already have passed through the region and would not be recorded by the Jason-1 altimeter. However the accurate numerical simulation of reflections and diffraction requires grid sizes (Stelling and Duinmeijer, 2003) of the order 100 m and can also be influenced by errors in bathymetry. Given these limitations it is encouraging that the broad peak from 2600–2900 km (due to reflection from Sumatra of the wave caused by uplift from 2.5–5° N) is resolved in Model 3 and the trough from 2900–3900 km in the Bay of Bengal (due to reflection and diffraction from the Nicobar and Andaman Islands) is partially resolved in Models 1, 2 and 5.

3.3. Defining the source region

A further analysis of Models 2 and 3 was carried out, in which the tsunami simulated by rupturing only the Northern and Southern sections of the fault (above/below 8° N for Model 2 and 6° N for Model 3), was investigated. The incident waves recorded by the altimeter in the South are caused by the southernmost part of the rupture, Fig. 3B. Whereas the northernmost incident peak and trough (at ~4700 and 4400 km), are only captured if the northern rupture data are included in Model 2. Note they are not reproduced by Model 3. Furthermore the southern patches of slip in Models 2 and 3 (Fig. 2) produce similar wave signatures in Fig. 3B, from the simulated peak at ~2000 km to the reflected peak at ~2600–2900 km.

The southern and northern patches of slip, with incident waves propagating to the south-west and originating from slip at ~2.5–5° N and ~6–7° N in Fig. 2, are responsible for the first and second simulated peak in Model 3 at ~2000 km and 2100 km, respectively. The double peak recorded by Jason-1 appears to be due to the above combination of incident waves. However, in order to reproduce the correct phase and amplitude of these incident waves, as recorded by Jason-1, both patches of slip should be displaced farther to the south-west and be of a larger magnitude. The origin of the peak recorded by Jason-1 at ~1900 km, is probably from a broad patch of slip from ~2–3.5° N, see Model 4, (Figs. 3A, S2 and S3). Whereas the observed peak at ~2050 km likely originates, from a substantial patch of slip from ~5–6° N, instead of the zone of zero slip presented in Model 3. This is consistent with Model 4, which also indicates substantial slip at ~5–6° N. Results from an earlier simulation (Ham, 2006), using a previous version of the fault model, also indicated that a large patch of slip, from ~4–6° N, does in fact reproduce the peak at ~2050 km and the trough at ~2250 km, as well as the reflected peak at ~2400 km. Finally, note the trough at ~2250 km, is well reproduced by Model 3, and is due to the arrival of incident waves associated with subsidence arising from both the southern (2.5–5° N) and northern (6–7° N) patches of slip. This is evident if one examines the separate northern and southern contributions to the tsunami waves in Fig. 3B.

The results from Models 1–5 indicate that the source of the tsunami originates from as far south as 2° N (Model 4, Fig. 3A). The modelled arrival times at Male, Diego Garcia and Gan Table 1, are in general agreement with a southern patch of slip from ~2–5° N. As are the arrival times at gauges to the west. Except for Model 4, all waves arrive at Tuticorin within a few minutes of the tide gauge arrival times and at Colombo somewhat earlier than recorded. Incident waves generated by both the northern and southern patches of slip in Model 2 arrive at Tuticorin and Colombo at the same time. In contrast waves from the north arrive earlier in Model 3; due to the greater extent of the northern slip in Model 3. The results from Model 2 (Fig. 3B) suggest that incident waves radiating from the northernmost patch of slip, from 8–10° N, lead to the peak at ~4700 km and the trough at ~4400. Note the peak at ~4200 km is also an incident wave but from the southern patch of slip. This is further supported by the arrival times at Vizakhapatnam, which are best represented by Models 2 and 5. Models 1, 3 and 4 arrive too early. Whereas waves arriving from slip due to the southern rupture arrive later in Models 2 and 3. The agreement of the modelled arrival times, from the northern ruptures of Models 2 and 3 with the Port Blair tide gauge data in Table 1, indicate that the leading tsunami wave arriving at Port Blair also originates from the northern slip. Model 3 does not reproduce the two northernmost peaks and the trough in Fig. 3A. The patch of slip from 10 to 14° N, offshore from the Andaman Islands, leads to the early arrival of the leading incident wave, Fig. 3B.

3.4. Temporal evolution of the tsunami

The temporal evolution of the rupture during the earthquake clearly has an important influence on the

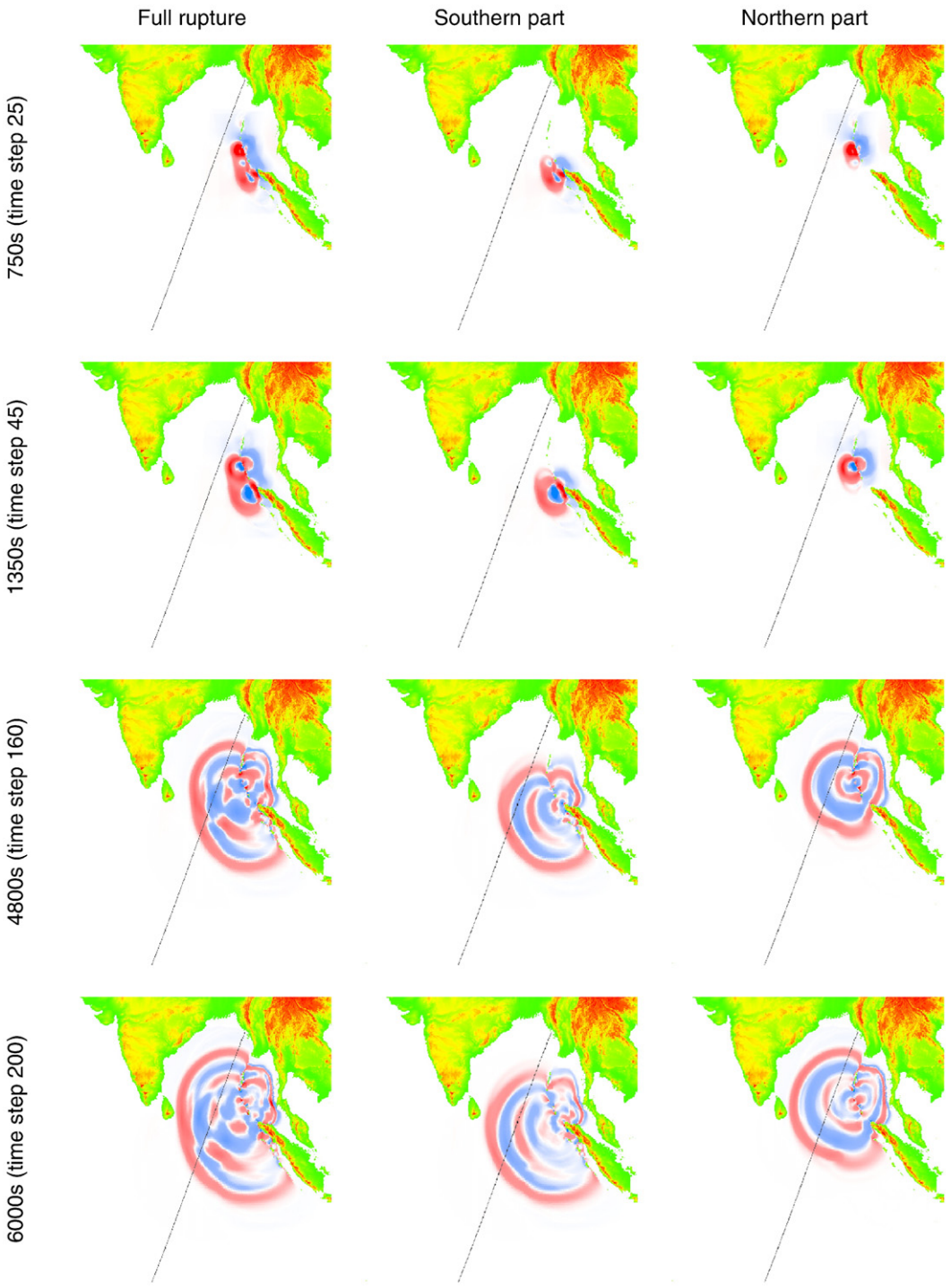

Fig. 4. Snapshots of the evolution of the sea surface elevation during the first 6000 s of the Indian Ocean Tsunami for the full rupture and the Southern and Northern ruptures only for Model 2. Red indicates an elevated sea surface, blue a depression. Note the tsunami waves radiating outward from the southern section of the fault and those originating from the northern section of the rupture. The tsunami waves appear to interfere constructively as they spread out over the Indian Ocean.

numerical results, Fig. 4. Starting in the south and ending less than 10 min later in the north the sea bed is uplifted on the western side of the fault and depressed on the eastern side; as further highlighted by Fig. S4, Supplementary Material. In the first 5–6 min the southern patch of slip of ~20 m generates a sea surface elevation to the west and a depression to the east, mimicking the shape of the ocean floor uplift and subsidence, Fig. 2. On the west side a wave of elevation radiates outwards in all directions and on the east a wave of depression.

In the next 4 min a second patch of slip of ~20 m centred near Car Nicobar (8–10° N) generates two more patches of sea surface displacement; again one of elevation to the west and one of depression to the east. From these radiate the incident tsunami waves that are recorded by the Jason-1 altimeter; the peak at ~4200 km, the trough at ~4400 km and the peak at ~4700 km. Note the agreement of Models 1, 2 and 5 with the altimeter data, Fig. 3A, and Model 2 northern rupture, Fig. 3B. This bi-modal slip distribution in the south–north direction with a slip minimum around 7–8° N, seems to be responsible for the generation of the two distinct south and north regions of tsunami wave generation, observed in Figs. 4 and S4, and in the animations (Movies 2–4, Supplementary Material). This is consistent with, the results of Models 2 and 3, Fig. 3B, discussed previously, indicating that a large patch of southern slip should extend northwards to ~6° N, and as also found in Ham (2006).

To the east, Fig. 4 shows the large depression in sea level propagating directly toward the Thai coast. The same patch of slip that caused the incident waves of elevation at ~1900 km and the depression at ~2000 km in the Jason-1 track is also responsible for the southern incident waves of depression and elevation that propagated to the east. Refraction by the bathymetry in the Andaman Sea appears to be responsible for the focussing of the tsunami from Khao Lak to Phi Phi Island. Finally one striking result that comes from rupturing the two sections separately is that the leading waves of the tsunami emanating from the south and from the north constructively interfere, see Fig. 4 and the animations (Movies 2–4, Supplementary Material). This is further supported by Table 1, with the northern and southern patches of slip in Model 2 arriving at Colombo and Tuticorin at the same time.

4. Discussion

Tsunami modelling and a comparison with sea level data, allows us to discriminate between the GPS slip inversion based on fault maps (Model 1) and the improved slip inversion using the aftershock data (Model 2); as well as between inversions supplemented by near field data Models 3–5. Model 3 provides a realistic upper bound to the moment magnitude (M_w 9.13). However, the inclusion of the northern near field data, degrades the modelled tsunami solution, suggesting these data also include a component of post-seismic deformation. Whereas the southern near field data, while extending the fault to the south and north (Model 5), are consistent with the continuous far field GPS data, (Model 2). However, while the Jason-1 data do not allow us to determine which of Models 2 and 5 better represents the slip distribution; the analysis of Models 1–5 provide important clues as to the likely slip distribution.

The largest patch of slip inverted from the co-seismic GPS data is located between 3–5° N, see Fig. 2 (Model 2). The missing peak (~1900 km) in the tsunami modelling results (Fig. 3A), suggests that the magnitude of the slip and uplift to the south–west of Sumatra has not been recovered by the co-seismic GPS inversions. Neither was it resolved by seismic data in Ammon et al. (2005). However, the further analysis presented here, in which the co-seismic far field data are supplemented by the near field data Models 3–5, does indicate a large patch of slip about 1° farther to the south–west. This is in agreement with the further analysis of seismic data by Song et al. (2005), as well as inverse numerical tsunami modelling based on tide gauge and satellite data, see Fine et al. (2005), Lay et al. (2005) and Vatvani et al. (2005). Model 5 inverts slip from 2.5–11° N which is in good agreement with these studies, as well as the more recent study by Fujii and Satake (2007). However, the analysis of the contributions of the southern and northern patches of slip in Model 3, indicate that there should be a substantial patch of slip extending northwards to ~6° N, which has not been inverted in either Models 2 or 5. In addition the southern slip should have a larger magnitude more like that recovered in Model 4.

When compared to other GPS based inversions of the co-seismic displacement (eg. Subarya et al., 2005; Chlieh et al., 2007; Rhie et al., 2007), our inversions show some similar patterns; the co-seismic displacements all show two distinct zones of slip, separated by an area of no or low slip corresponding to the zone where the rupture speed decreases (Vigny et al., 2005) and that may act as a seismological barrier. The results from Model 2 suggest that the likely source of the Indian Ocean Tsunami consists of two distinct patches of north and south slip separated by a zone of minimal slip at ~7–8° N. In

agreement with reverse modelling studies (Fine et al., 2005; Vatvani et al., 2005), we find that the northern source of incident tsunami waves recorded by Jason-1, radiate outwards from the northern patch of slip from 8–10° N. The earthquake magnitude obtained by our models ranges between M_w 9.08 and 9.13. Although some studies infer a significantly higher magnitude ($M_w \sim 9.2$–9.3) (eg. Ishii et al., 2005; Banerjee et al., 2007), our estimate of the magnitude is consistent with the lower bound of the magnitudes obtained by both seismologic (eg. Ammon et al., 2005) geodetic (eg. Chlieh et al., 2007) and seismo-GPS combined models (Rhie et al., 2007).

Models 3 and 4 demonstrate that slip, associated with offshore uplift to the west of the Andaman Islands, cannot extend to 14° N. Tsunami waves originating from such an offshore source degrade the agreement with the Jason-1 incident waves in the north, as well as the reflected waves at 2900–3900 km and the arrival times recorded by the tide gauges. However, Model 1 and results in Ham (2006), allow the possibility of slip until 12° N if the uplift is displaced, eastwards of that found in Models 3 and 4, towards the Andaman Islands. Moreover the location of the pivot line is affected by the inclusion of the northern near field data; Gahalaut et al. (2006) and Bilham et al. (2005). In particular, the island of Little Andaman uplifts in Models 1, 2 and 5; while it subsides in Models 3 and 4. According to Meltzner et al. (2006), the subsidence of Little Andaman that arises from the Gahalaut et al. (2006) data, is not realistic.

It is worth commenting that Ammon et al. (2005) found three distinct bursts of energy at 4–6° N, 8–10° N and 12–13.75° N, which they attributed to patches of high slip, although the northernmost limit of slip that fits the peak, trough and peak sequence in the north, in Model 1 and Ham (2006), is located 1° south of theirs. Additionally Ishii et al. (2005) found distinct bursts of energy at about 60 s (~3° N), 120 s (~5° N) and 300 s (~8–10° N), with a minimum at 240 s (~7° N) and with diminishing intensity to about 12° N. The kinematic GPS analysis has all co-seismic motion ceasing at about 12° N. The Jason-1 data is the best data set with which to validate the simulated tsunami arrival times in the north. The survey reports for Myanmar give conflicting arrival times and the data from Bangladesh are not available. However, the Jason-1 data do not allow us to determine if slip only extends to 10° N as found in Model 2, or whether it extends as far north as 12° N, as found in Model 1 and Ham (2006). Assuming the tsunami is generated by co-seismic motion, the results of Models 2, 3 and 5 suggest the magnitude of the earthquake to be $M_w \sim 9.1$ ($9.08 < M_w < 9.13$).

The agreement in the north (Models 1, 2 and 5) of both the phase and amplitude of the incident waves with the Jason-1 data, suggests that the timing, as derived from the kinematic analysis of the GPS data, is fairly accurate. It is certainly within the constant rupture speed range of 2.3–2.8 km s^{-1} found by Ammon et al. (2005), Ishii et al. (2005), Lay et al. (2005). In contrast, studies by de Groot-Hedlin (2005) and Krüger and Ohrnberger (2005), indicate two distinct phases to the rupture, but with comparable mean rupture speeds. Furthermore, these results support the rapid slip hypotheses, see Ishii et al. (2005), Krüger and Ohrnberger (2005), Ni et al. (2005). Results from the first analysis of the GPS data, the Hi-Net array and the German array suggest substantial rapid slip of about 20 m extending to the Andaman Islands, consistent with geodetic observations of island uplift and subsidence, Neetu et al., 2005.

Our models predict tsunami waves around the Bay of Bengal, however, our results suggest that the unusually large devastation recorded around Sri Lanka, along the southern Indian Coast and Thailand was due to the constructive interference of the incident waves radiating outwards in the first 5–6 min from this southern patch of slip and then in the next 4 min from the northern patch of slip. Notably as discussed by Bilham et al. (2005) there is no historic evidence of a tsunami in the Bay of Bengal of similar magnitude.

5. Conclusions

Our results suggest that GPS analysis, in combination with tsunami modelling and sea level data, is a powerful tool with which to gain insight into the seismic rupture process and the consequences of its timing. This is the first time such an approach has been used. The new fault geometry based on the aftershock data gave an improved agreement between the modelled tsunami waves and the altimetry data. We conclude that rapid slip in both the south and the north appears to account for the incident waves recorded by the Jason-1 altimeter. The large waves generated in the south are correlated with the patch of slip of order 20 m off Sumatra. The patch of order 20 m slip, extending from Katchell Island in the Nicobars to Little Andaman, is responsible for the northern waves. It is evident that both the north and south sections act as significant tsunami wave generating sources and that the resulting constructive interference pattern contributed to the enormous tsunami off Sri Lanka and Southern India.

Finally the GPS data could be automatically processed and inverted to provide initial surface displacement fields within 15–30 min. Consequently

they could already be a valuable component of an Indian Ocean tsunami forecasting system. It is clear that even the first model inversion, based on the available fault maps, was enough to issue a warning if an operational GPS based system had been in place. Indeed the same regional GPS systems and analysis could be set up in other areas of the world, in order to supplement traditional seismic based tsunamis forecasting systems.

Acknowledgements

We thank the SEAMERGES (http://www.deos.tudelft.nl/seamerges) project, funded by the ASEAN-EU University Network Programme (AUNP) and also the different national agencies (DSMM-Malaysia, RTSD-Thailand and BAKOSURTANAL-Indonesia) for sharing their regional GPS data. We also gratefully acknowledge the contributions of the many participants in the SEAMERGES project, with out whom this research would not have been possible. We are very grateful to Robert McCaffrey for allowing us to use DEFNODE software he developed at RPI. We would like to thank Dr. Rabinovich (IOS) and Dr. Thomson (IOS) for providing us with a copy of their recent paper using tide gauge data and Prof. Chari Pattiarachi (UNSW) for providing us with new tide gauge data for Sri Lanka. We would like to thank Prof. Burgmann (UC Berkeley) and an anonymous reviewer for their invaluable comments which substantially improved this paper.

Appendix A. Supplementary data

Supplementary data associated with this article can be found, in the online version, at doi:10.1016/j.epsl.2007.06.002.

References

Abercrombie, R.E., Antolik, M., Ekstrom, G., 2003. The June 2000 M_w 7.9 earthquakes south of Sumatra: deformation in the India–Australia Plate. J. Geophys. Res. 108, 2018. doi:10.1029/2001JB000674.

Ammon, C.J., Ji, C., Thio, H.K., Robinson, D., Ni, S., Hjorleifsdottir, V., Kanamori, H., Lay, T., Das, S., Helmberger, D., Ichinose, G., Polet, J., Wald, D., 2005. Rupture process of the 2004 Sumatra–Andaman Earthquake. Science 308, 1133–1139.

Banerjee, P., Pollitz, F.F., Burgmann, R., 2005. The size and duration of the Sumatra–Andaman Earthquake from far-field static offsets. Science 308, 1769–1772.

Banerjee, P., Pollitz, F.F., Nagarajan, B., Burgmann, R., 2007. Coseismic slip distributions of the 26 December 2004 Sumatra–Andaman and 28 March 2005 Nias Earthquakes. Bull. Seismol. Soc. Am. 97, S86–S102. doi:10.1785/0120050609.

Bilham, R., 2005. A flying start, then a slow slip. Science 308, 1126–1127.

Bilham, R., Engdahl, R., Feldl, N., Satyabala, S.P., 2005. Partial and complete rupture of the Indo-Andaman plate boundary 1847–2004. Seismol. Res. Lett. 76, 299–311.

Briggs, R.W., Sieh, K., Meltzner, A.J., Natawidjaja, D., Galetzka, J., Suwargadi, B., Hsu, Y., Simons, M., Hananto, N., Suprihanto, I., Prayudi, D., Avouac, J.P., Prawirodirdjo, L., Bock, Y., 2006. Deformation and slip along the Sunda Megathrust in the great 2005 Nias–Simeulue Earthquake. Science 311, 1897–1901.

Bürgmann, R., Ergintav, S., Segall, P., Hearn, E.H., McClusky, S., Reilinger, R.E., Woith, H., Zschau, J., 2002. Time-dependent distributed afterslip on and deep below the Izmit earthquake rupture. Bull. Seismol. Soc. Am. 92, 126–137.

Chamot-Rooke, N., Jestin, F., de Voogd, B., Diebold, J., Dyment, J., Farcy, F., Fleitout, L., Huchon, P., Liverpool, P., Munschy, M., Oshida, A., Royer, J.Y., Truffert, C., Weissel, J.K., Ziolkowski, A., 1993. Intraplate shortening in the central Indian Ocean determined from a 2100-km-long north–south deep seismic reflection profile. Geology 21, 1043–1046.

Chlieh, M., Avouac, J.P., Hjorleifsdottir, V., Song, T.R.A., Ji, C., Sieh, K., Sladen, A., Hebert, H., Prawirodirdjo, L., Bock, Y., Galetzka, J., 2007. Coseismic slip and afterslip of the great M_w 9.15 Sumatra–Andaman Earthquake of 2004. Bull. Seismol. Soc. Am. 97, S152–S173. doi:10.1785/0120050631.

Curray, J.R., 1989. The Sunda Arc — a model for oblique plate convergence. Neth. J. Sea Res. 24, 131–140.

de Groot-Hedlin, C.D., 2005. Estimation of the rupture length and velocity of the Great Sumatra earthquake of Dec 26, 2004 using hydroacoustic signals. Geophys. Res. Lett. 32, L11303. doi:10.1029/2005GL022695.

Deplus, C., 2001. Plate tectonics: Indian ocean actively deforms. Science 292, 1850–1851.

Deplus, C., Diament, M., Hébert, H., Bertrand, G., Dubois, J., Malod, J., Patriat, P., Pontoise, B., Sibilla, J.-J., 1998. Direct evidence of active deformation in the eastern Indian oceanic plate. Geology 26, 131–134.

Dziewonski, A.M., Anderson, D.L., 1981. Preliminary reference earth model. Phys. Earth Planet. Inter. 25, 297–356. doi:10.1016/0031-9201(81)90046-7.

Fine, I.V., Rabinovich, A.B., Thomson, R.E., 2005. The dual source region for the 2004 Sumatra tsunami. Geophys. Res. Lett. 32, L16602.

Fitch, T.J., 1972. Plate convergence, transcurrent faults, and internal deformation adjacent to Southeast Asia and Western Pacific. J. Geophys. Res. 77, 4432.

Fujii, Y., Satake, K., 2007. Tsunami source of the 2004 Sumatra–Andaman Earthquake inferred from tide gauge and satellite data. Bull. Seismol. Soc. Am. 97, S192–S207. doi:10.1785/0120050613.

Gahalaut, V.K., Nagarajan, B., Catherine, J.K., Kumar, S., 2006. Constraints on 2004 Sumatra–Andaman Earthquake rupture from GPS measurements in Andaman–Nicobar Islands. Earth Planet. Sci. Lett. 242, 365–374.

Genrich, J.F., Bock, Y., McCaffrey, R., Prawirodirdjo, L., Stevens, C.W., Puntodewo, S.S.O., Subarya, C., Wdowinski, S., 2000. Distribution of slip at the northern Sumatran fault system. J. Geophys. Res. 105, 28327–28341.

Gower, J., 2007. The 26 December 2004 tsunami measured by satellite altimetry. Int. J. Remote Sens. 28, 2897–2913.

Ham, D.A., 2006. On techniques for modelling coastal and ocean flow with unstructured meshes. PhD Thesis, pp. 121, Delft University of Technology, The Netherlands.

Ham, D., Pietrzak, J.D, Stelling, G.S., 2005. A scalable unstructured grid 3-dimensional finite volume model for the shallow water equations. Ocean Model. 10, 153–169.

Ishii, M., Shearer, P.M., Houston, H., Vidale, J.E., 2005. Extent, duration and sped of the 2004 Sumatra–Andaman Earthquake imaged by the hi-net array. Nature 435, 933–936.

Krüger, F., Ohrnberger, M., 2005. Tracking the rupture of the M_w 5 9.3 Sumatra earthquake over 1150 km at teleseismic distance. Nature 435, 937–939.

Labeur, R.J., Pietrzak, J.D., 2005. A fully three dimensional unstructured grid non-hydrostatic finite element coastal model. Ocean Model. 10, 51–67.

Lay, T., Kanimori, H., Ammon, C.J., Nettles, M., Ward, S.N., Aster, R.C., Beck, S.L., Bilek, S.L., Brudzinski, M.R., Butler, R., DeShon, H.R., Ekstrom, G., Satake, K., Sipkin, S., 2005. The great Sumatra–Andaman Earthquake of 26 December 2004. Science 308, 1127–1133.

McCaffrey, R., 1991. Slip vectors and stretching of the Sumatran Fore Arc. Geology 19, 881–884.

McCaffrey, R., 1995. DEFNODE Users' Guide. Rensselaer Polytechnic Institute, New York. http://www.rpi.edu/~mccafr/defnode.

McCaffrey, R., 2002. Crustal block rotations and plate coupling in Plate Boundary Zones. In: Stein, S., Freymueller, J. (Eds.), Geodynamics Series, vol. 30. American Geophysical Union, Washington DC, pp. 101–122.

McCaffrey, R., 2005. Block kinematics of the Pacific–North America plate boundary in the southwestern US from inversion of GPS, seismological, and geologic data. J. Geophys. 110.

McCaffrey, R., Zwick, P.C., Bock, Y., Prawirodirdjo, L., Genrich, J.F., Stevens, C.W., Puntodewo, S.S.O., Subarya, C., 2000. Strain partitioning during oblique plate convergence in northern Sumatra: geodetic and seismologic constraints and numerical modeling. J. Geophys. Res. 105, 28363–28376.

Meltzner, A.J., Sieh, K., Abrams, M., Agnew, D.C., Hudnut, K., Avouac, J.P., Natawidjaja, D., 2006. Uplift and subsidence associated with the great Aceh–Andaman Earthquake of 2004. J. Geophys. Res. 111. doi:10.1029/2005JB003891.

Merrifield, M.A., Firing, Y.L., Aarup, T., Agricole, W., Brundrit, G., Chang-Seng, D., Farre, R., Kilonsky, B., Knight, W., Kong, L., Magori, C., Manurung, P., McCreery, C., Mitchell, W., Pillay, S., Schindele, F., Shillington, F., Testut, L., Wijeratne, E.M.S., Caldwell, P., Jardin, J., Nakahara, S., Porter, F.Y., Turetsky, N., 2005. Tide gauge observations of the Indian Ocean tsunami, December 26, 2004. Geophys. Res. Lett. 32, L09603. doi:10.1029/2005GL022610.

Nedimovic, M.R., Hyndman, R.D., Ramachandran, K., Spence, G.D., 2003. Reflection signature of seismic and aseismic slip on the northern Cascadia subduction interface. Nature 424, 416–420.

Neetu, S., Suresh, I., Shankar, R., Shankar, D., Shenoi, S.S.C., Shetye, S.R., Sundar, D., Nagarajan, B., 2005. Comment on the great Sumatra–Andaman Earthquake of 26 December 2004. Science 310, 1431a. doi:10.1126/science.1118950.

Ni, S., Kanimori, H., Helmberger, D., 2005. Energy radiation from the Sumatra earthquake. Nature 434, 582.

Nielsen, C., Chamot-Rooke, N., Rangin, C., 2004. From partial to full strain partitioning along the Indo-Burmese hyper-oblique subduction. Mar. Geol. 209, 303–327.

Okada, Y., 1985. Surface deformation due to shear and tensile faults in a half-space. Bull. Seismol. Soc. Am. 75, 1135–1154.

Okada, Y., 1992. Internal deformation due to shear and tensile faults in a half-space. Bull. Seismol. Soc. Am. 82, 1018–1040.

Park, J., Song, T.A., Tromp, J., Okal, E., Stein, S., Roult, G., Clevede, E., Laske, G., Kanamori, H., Davis, P., Berger, J., Braitenberg, C., Camp, M., Lei, X., Sun, H., Xu, H., Rosat, S., 2005. Earth's free oscillations excited by the 26 December 2004 Sumatra–Andaman Earthquake. Science 308, 1139–1144.

Pattiarachi, C., 2005. Tsunami impacts on Sri Lanka-lessons for disaster reduction on coasts. Int. Symposium Disaster Reduction on Coasts, Monash University, Australia, pp. 1–10.

Pietrzak, J., Iskandarani, M., Schröter, J., Lyard, F., 2004. Editorial Special Issue: the third international workshop on unstructured mesh numerical modelling of coastal, shelf and ocean flows Toulouse, France, September 20–September 22, 2004. Ocean Model. 15, 1–2.

Pietrzak, J., Deleersnijder, E., Schröter, J., 2005. Editorial Special Issue: the second international workshop on unstructured mesh numerical modelling of coastal, shelf and ocean flows Delft, The Netherlands, September 23–September 25, 2003. Ocean Model. 10, 1–3.

Prawirodirdjo, L., Bock, Y., McCaffrey, R., Genrich, J., Calais, E., Stevens, C., Puntodewo, S.S.O., Subarya, C., Rais, J., 1997. Geodetic observations of interseismic strain segmentation at the Sumatra subduction zone. Geophys. Res. Lett. 24, 2601–2604.

Press, W.H., Flannery, B.P., Teukolsky, S.A., Vetterling, W.T., 1989. Numerical Recipes. Cambridge Univ. Press, New York.

Pubellier, M., Ego, F., Chamot-Rooke, N., Rangin, C., 2003. The building of pericratonic mountain ranges: structural and kinematic constraints applied to GIS-based reconstructions of SE Asia. Bull. Soc. Geol. Fr. 174, 561–584.

Rabinovich, A.B., Thomson, R.E., 2007. The 26 December 2004 Sumatra tsunami: analysis of tide gauge data from the World Ocean Part 1. Indian Ocean and South Africa. Pure Appl. Geophys. 164, 261–308.

Rhie, J., Dreger, D., Burgmann, R., Romanowicz, B., 2007. Slip of the 2004 Sumatra–Andaman Earthquake from joint inversion of long-period global seismic waveforms and GPS static offsets. Bull. Seismol. Soc. Am. vol. 97 (1A), S115–S127. doi:10.1785/0120050620.

Schroeter, J., Sein, D., Taguchi, E., Sidorenko, D., Danilov, S., Braune, S., 2006. The modelling concept of the German–Indonesian Tsunami Early Warning System GITEWS. Geophys. Res. Abstr. 8, 08929.

Simons, W.J.F., Socquet, A., Vigny, C., Ambrosius, B.A.C., Haji Abu, S., Chaiwat Promthong, Subarya, C., Sarsito, D.A., Matheussen, S., Morgan, P., Spakman, W., in press. A Decade of GPS in SE Asia: Resolving Sundaland Motion and Boundaries J. Geophys. Res.,112, B0XXXX. doi:10.1029/2005JB003868.

Socquet, A., Vigny, C., Chamot-Rooke, N., Simons, W., Rangin, C., Ambrosius, B., 2006. India and Sunda plates motion and deformation along their boundary in Myanmar determined by GPS. J. Geophys. Res. 111, B05406. doi:10.1029/2005JB003877.

Stein, S., Okal, E.A., 2005. Speed and size of the Sumatra earthquake. Nature 434, 581–582.

Stelling, G.S., Duinmeijer, S.P.A., 2003. A staggered conservative scheme for every Froude number in rapidly varied shallow water flows. Int. J. Numer. Methods Fluids 43, 1329–1354.

Song, Y.T., Ji, C., Fu, L.L., Zlotnicki, V., Shum, C.K., Yi, Y., Hjorleifsdottir, V., 2005. The 26 December 2004 tsunami source estimated from satellite radar altimetry and seismic waves. Geophys. Res. Lett. 32, L20601. doi:10.1029/2005GL023683.

Subarya, C., Chlieh, M., Prawirodirdjo, L., Avouac, J.P., Bock, Y., Sieh, K., Meltzner, A.J., Natawidjaja, D.H., McCaffrey, R., 2005. Plate-boundary deformation associated with the great Sumatra–Andaman Earthquake. Nature 440, 46–51.

Titov, V., Rabinovich, A.B., Mofjeld, H.O., Thomson, R.E., Gonzalez, F.I., 2005a. The global reach of the 26 December 2004 Sumatra tsunami. Science 309, 2045–2048.

Titov, V., Gonzalez, F.I., Bernard, E.N., Bernard, E.N., Eble, M.C., Mofjeld, H.O., Newman, J.C., Venturato, A.J., 2005b. Real-time tsunami forecasting: challenges and solutions. Nat. Hazards 35, 35–41.

Vatvani, D., Schrama, E., van Kester, E.J., 2005. Hindcast of tsunami flooding in Aceh — Sumatra, Proceedings Waves Conference 2005. The Fifth International Symposium on Ocean Wave Measurements and Analysis, Madrid, Spain 3th – 7th July 2005.

Vigny, C., Simons, W.J.F., Abu, S., Bamphenyu, R., Satirapod, C., Choosakul, N., Subarya, C., Socquet, A., Omar, K., Abidin, H.Z., Ambroius, B.A.C., 2005. Insight into the 2004 Sumatra–Andaman Earthquake from GPS measurements in southeast Asia. Nature 436, 201–206.

Walters, R., 2006. Design considerations of a finite element coastal ocean model. Ocean Model. 15, 90–100.

Wijeratne, E.M.S., Pattiarachi, C., 2005. Characteristics of 26 Dec 2004 and 28 March 2005 Tsunami Waves Oscillations Along the Coast of Sri Lanka, Asian Pacific Coasts 2005, Juju, Korea.